Co-actuation: A Method for Achieving High Stiffness and Low Inertia for Haptic Devices

Ruihang Chu, Yuru Zhang, *Senior Member, IEEE*, Hongdong Zhang, Weiliang Xu, *Senior Member, IEEE*, Jee-Hwan Ryu, *Member, IEEE* and Dangxiao Wang, *Senior Member, IEEE*

Abstract—Achieving high stiffness and low inertia is a big challenge for current haptic devices. Impedance-based devices are limited in providing high stiffness while, in contrast, admittance-based devices are limited in generating low inertia. Thus, it is difficult to simulate hard contact and small inertia simultaneously in virtual environments. In this paper, we introduce a co-actuation module to overcome this difficulty. The module is a one degree-of-freedom (DOF) revolute joint which consists of a link and a physical constraint with a clearance between the two components. A motor controls the physical constraint moving cooperatively with the link. In free space, the constraint has no contact to the link and thus, users can move the link freely without feeling the inertia of the motor. In constrained space, the constraint comes into contact with the link and thus, users can feel a resistance from the motor. By means of a direct physical contact between the link and the constraint, users can feel a hard virtual surface. This paper describes the principle and the implementation of the proposed co-actuation module. Performance evaluation was conducted using a two-DOF haptic device in a task workspace of 100 mm × 100 mm. The effective inertia of the device is 64-142 g within the task workspace. The device can stably render a virtual wall with stiffness as high as 65 N/mm. The penetration to the virtual wall was 0.02-0.41 mm when tapping the wall with a speed range of 80-320 mm/s. The maximum back driving force was about 0.19 N when moving within 4.5-8.6 mm/s. The experimental results demonstrate that the concept of co-actuation is feasible in achieving high force, high stiffness range and low inertia for haptic devices.

Index Terms—Co-actuation, haptic device, force feedback, physical constraint, stiffness rendering, transparency

——————————— ◆ ———————————

1 INTRODUCTION

A great number of haptic devices have been developed which allow users to feel the feedback force from both virtual and remote physical environments [1-4]. Existing haptic devices can be divided into two distinct classes, impedance and admittance displays. Impedance displays usually have low inertia and friction, and are highly back-drivable [1], [2]. They typically are able to render low-inertia, low-damping environments, but have difficulty emulating stiff constraints. Notable impedance devices, Phantom models, have a low inertia about 50 g. However, the stiffness they can render is low, ranging from 1 to 3.5 N/mm [5]. Admittance displays usually contain a reducer of a significant ratio, and are therefore non-back-drivable due to high inertia and friction [3], [4]. They are capable of rendering high stiffness and large damping, but often not capable of rendering low inertia. Notable admittance device, Haptic Master, can render stiffness as high as 50

N/mm and the nominal/max force of 100/250 N, while the minimal tip inertia is 2 kg [3].

In some applications, such as dental simulation [6], the enamel is highly stiff and the dental tools are light. Thus, both high stiffness and low inertia are required, which places a great challenge in the design of force feedback devices. Previous research has suggested that stiffness higher than 24 N/mm is required to convey the presence of a hard constraint [7]. In the current commercial force feedback devices, either impedance or admittance haptic devices are unable to achieve the stiffness higher than 24 N/mm, while having inertia lower than 10 g for simulating the dental tools.

Several researchers studied the maximum stiffness an impedance display can stably render. Colgate and Schenkel developed a relationship between damping, stiffness, and update rate from which the maximum stiffness of a virtual wall can be estimated [8]. More recently, the relationship was generalized by considering more factors including sensor quantization and coulomb friction [9-11].

Numerous research efforts were made in the emulation of hard virtual surface. Different concepts have been proposed to implement a truly "hard" constraint. To render stiff environments over a large workspace, Zinn et al. [12] addressed the limitation of traditional impedance devices by introducing a new actuation approach based on parallel actuation concept. They divided the torque generation into separate low- and high-frequency actuators that work in parallel. A high-power, high-torque actuator was used to

————————————————

- *R. Chu, Y. Zhang, H. Zhang and D. Wang are with the State Key Lab of Virtual Reality Technology and Systems and Beijing Advanced Innovation Center for Biomedical Engineering, Beihang University, No. 37 Xueyuan Road, Haidian District, 100191, Beijing, China. Email: churuihang@buaa.edu.cn, yuru@buaa.edu.cn, izhang-hd@163.com, hapticwang@buaa.edu.cn.*
- *D. Wang is also with Peng Cheng Laboratory, Shenzhen, Guangdong Province, 518055, China.*
- *W. Xu is with the Department of Mechanical Engineering, The University of Auckland, 20 Symonds Street, Auckland, New Zealand. Email: p.xu@auckland.ac.nz.*
- *Jee-Hwan Ryu is with the School of Mechanical Engineering, Korea University of Technology and Education, Cheonan 330-708, South Korea. Email: jhryu@koreatech.ac.kr.*
- *Corresponding author: Dangxiao Wang.*

provide the low frequency torques while a small, fast actuator was used to provide the high frequency torques. They also optimized the locations of the low- and high-frequency actuators on the device, so that their effect on device transparency was minimized while their contribution to dynamic force range was maximized. Experimental data showed that the approach was able to achieve a high stiffness of 57 N/mm for a three-DOF prototype and reduce the output friction to less than 1.5 N within a large workspace of 0.6 m³.

Being dissipative by nature, brakes are ideal for provision of physical damping to a haptic device. Several researchers have investigated the use of brakes to achieve high impedance and thus improve stability. Different types of brakes were used [13-17]. It was found that some characteristics of the brakes, such as being slow to actuate and nonlinear relationship between velocity and torque, limit the fidelity of the rendering.

To improve the performance of virtual wall rendering, Gosline and Hayward proposed to use eddy current brakes (ECBs) as linear, fast actuating, programmable viscous dampers for haptic rendering. They found that virtual walls rendered using the physical dampers do not have the characteristic "sticky" feel that is typical of walls rendered using existing programmable brakes. However, the use of dampers in brakes leads to the increase of the inertia and power consumption in the device [18]. In an alternative approach, the dissipative properties of a DC motor were taken as an advantage to realize programmable electrical damping [19]. Diolaiti and Niemeyer proposed wave haptics approach to fully embrace and utilize the electrical dynamics of DC motors [20]. Their approach was built upon the motor's physical behavior and can achieve higher virtual stiffness than traditional rendering methods for impedance displays.

Another concept to provide a convincingly hard surface is to use mechanical constraints. A typical example was Cobot, in which a parallel linkage was used to build a 6 DOF device [4]. Although controlled as an admittance device, the Cobot does not suffer from the high inertia, friction and backlash that normally exist in a highly geared admittance device. By using a rotational-to-linear continuously variable transmission (CVT), the Cobot enhanced the dynamic range that extends continuously from a completely clutched state to a highly back drivable state. With the novel mechanical design, the Cobot achieved a force transmission capability exceeding 50 N, a structural stiffness ranging from 20 to 400 N/mm, a motion control bandwidth of 40 Hz, and the near zero power requirements for sustaining high output loads.

An early concept using mechanical constraints is encounter-type force feedback device [21], which stays nearby the interaction location and waits for an operator to encounter it. Yokokohji et al. [22] proposed an encounter-type haptic device to simulate three-fingered grasping process, extending the concept to fingertip contacts. With the observation from actual human grasping, the mecha-

nism of the device was designed. Then, an encounter-type master hand, featured with a compact exoskeleton mechanism, was introduced in [23] to enable free motion of the operator's finger and natural contact sensation at the fingertip. A further variation on mechanical constraints is dynamic physical constraints (DPC) introduced recently by [24]. The DPC is adjusted depending on the user's current position in space. When not in contact with the virtual surface, the user can move the device with complete freedom as all joints are unimpeded. Once the virtual surface is reached, the DPC creates a unidirectional physical barrier to limit the movement of partial joints. The DPC concept can produce a realistic sensation of hard surface contact because of the real physical contact between the user and the DPC. However, the DPC concept was proposed to emulate a virtual surface that is approximately concentric with the central pivot point. The extension of this idea to arbitrary virtual surfaces needs further investigation.

To develop a haptic device that can render both low inertia and high stiffness, it is necessary to overcome the limitations of impedance displays in rendering high stiffness and admittance displays in rendering low inertia. We proposed a concept, co-actuation, to achieve this goal in [25]. Preliminary study on a 1 DOF device showed that the co-actuation approach is effective in achieving high stiffness while keeps low inertia of force feedback devices [26]. In this paper, we prove that the co-actuation approach can be applied to multi-DOF haptic devices. In Section II, we describe briefly the principle of co-actuation approach. In Section III, we present a model for determining a critical design parameter of the approach. In Section IV, we discuss in details about controller implementation. In Section V we evaluate the performance of the co-actuation approach using a 2 DOF haptic device. We conclude in Section VI.
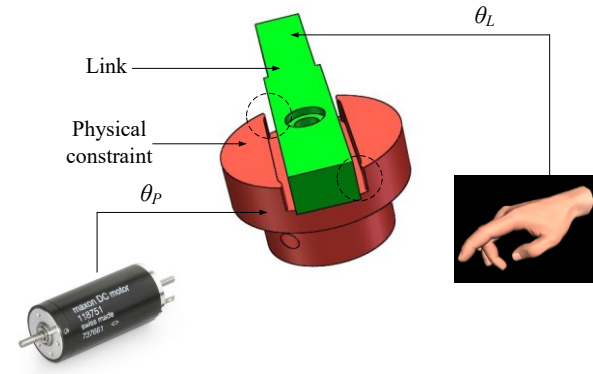
2 CO-ACTUATION PRINCIPLE

Co-actuation means that the actuators of the force feedback device act in collaboration with the user. Fig. 1 (a) shows the principle of co-actuation in a 1 DOF module, in which the link is actuated by the user and the socket by the motor. The socket works as a physical constraint. The link and the socket rotate about the same axis and are defined as θ_L and θ_P respectively. The two angles have the same home position, as shown in Fig. 1 (b). Given an arbitrary θ_P, the rotation range of the link limited by two sides of the socket is determined by a clearance angle, which is defined as
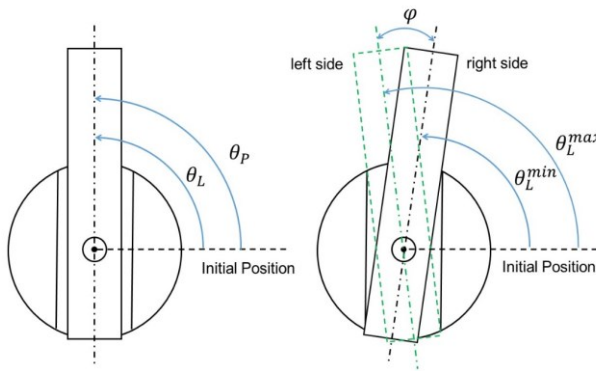
$$\varphi = \left| \theta_L^{\max} - \theta_L^{\min} \right|, \quad \text{given a } \theta_P \tag{1}$$

Note that the clearance angle φ is a structural constant and it is shown in Fig. 1 (b).
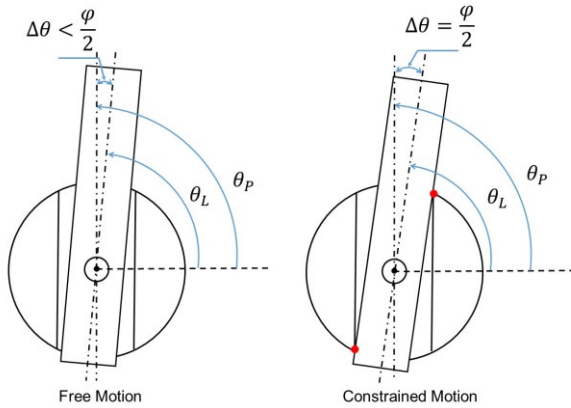
The module works in two modes: free motion and constrained motion, which are distinguished by

(a)

(b)

(c)

Fig. 1. (a) Working principle of co-actuation. (b) Definition of the link position θ_L, the physical constraint position θ_P and the clearance angle φ. (c) Definition of the free motion and the constrained motion.

$$\Delta\theta = |\theta_L - \theta_P| = \begin{cases} [0, \dfrac{\varphi}{2}) & \text{Free motion} \\[2ex] \dfrac{\varphi}{2} & \text{Constrained motion} \end{cases} \qquad (2)$$

In free motion mode, the physical constraint continuously tracks the rotation of the link ensuring that the link is not in contact with the socket. Thus, the motion of the link is unimpeded by the physical constraint. In constrained motion mode, the motion of the link is impeded by the socket through the two physical contacts between them. Two modes are depicted in Fig. 1 (c).
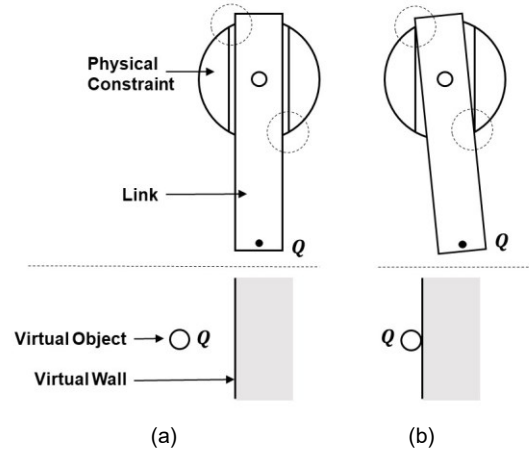

Fig. 2. (a) Motion mapping between the link and the virtual object in free motion mode. (b) Motion mapping between the link and the virtual object in constrained motion mode.

Fig. 2 (a) and (b) show how the two modes are mapped to the virtual environment. In Fig. 2 (a), the module works in free motion mode. Accordingly, the virtual object moves freely in the virtual environment without contact with the virtual wall. In Fig. 2 (b), the module works in constrained motion mode. Accordingly, the virtual object collides with the virtual wall.

In co-actuation approach, the inertia reflected to the user is given by

$$J = J_{link} \qquad (3)$$

where J_{link} is the link inertia. This is because the link and the socket/motor are mechanically decoupled. In other existing haptic devices, the two are mechanically coupled, thus the effective inertia is given by

$$J = J_{link} + J_{socket} + J_{transmission} + i^2 \cdot J_{motor} \qquad (4)$$

where J_{socket}, $J_{transmission}$, J_{motor} are the inertias of the socket, the transmission and the motor respectively, i is the transmission ratio. Compared to the coupled situation, the inertia in the co-actuation is reduced to a fraction defined by the ratio

$$\eta = \frac{J_{link}}{J_{link} + J_{socket} + J_{transmission} + i^2 \cdot J_{motor}} \qquad (5)$$

When simulating high stiffness, the large motor and high transmission ratio are required to provide a large force, which leads to the increased inertia of motor and transmission. Because of the mechanical decoupling, the increased inertia and friction in transmission is not reflected to the user and in this way both high stiffness and low inertia/friction can be achieved with the co-actuation approach.

The effectiveness of the co-actuation approach was verified through a 1 DOF module in [25]. Here we briefly report the result. More details about the experiment process can be found in [25]. As shown in Fig. 3, the physical constraint was actuated by a motor (Maxon RE30) with a gear ratio of 50. Two optical encoders are respectively mounted on the shafts of the motor and the link to measure their positions. At the tip of the link, a force sensor (ATI Nano 17) is mounted to measure the force applied
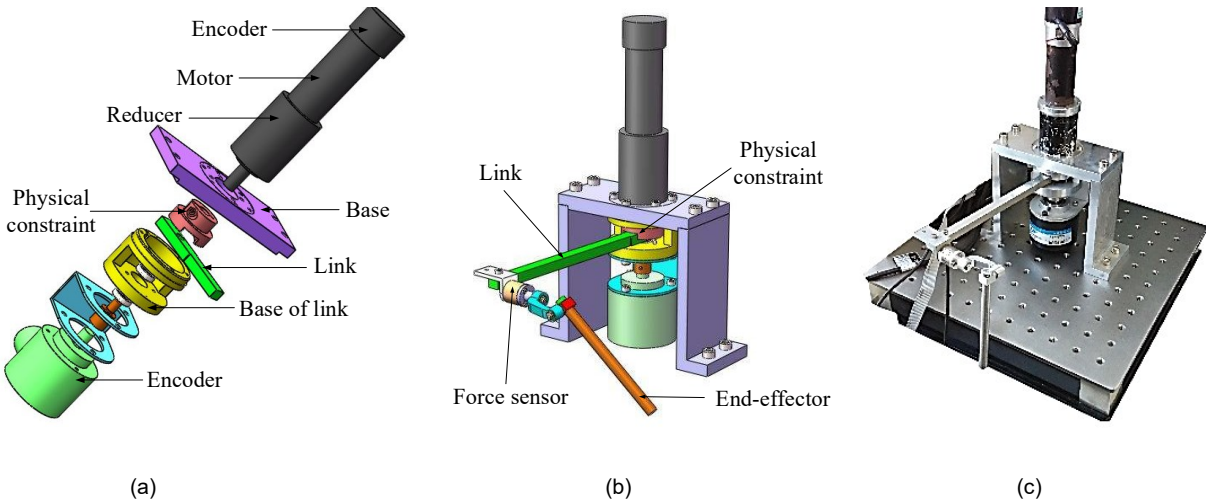
Fig. 3. 1 DOF co-actuation module. (a) The structural components. (b) The virtual prototype. (c) The physical prototype.

TABLE I   PARAMETERS OF THE CO-ACTUATION MODULE

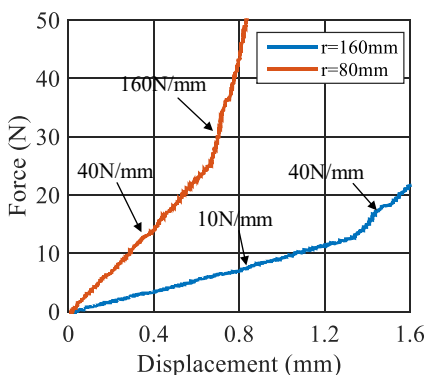| Parameter	Value
Motor	Maxon RE30 268214
Reduction	HD CSF11, ratio i=50
Force sensor	ATI Nano 17, res. 0.001N
Encoders	res. 0.036° (motor), 0.005° (link)
Driver	Custom designed
Close-loop rate	1kHz

Fig. 4. Virtual wall stiffness simulated by a 1 DOF co-actuation module. ([25])

3   CLEARANCE MODEL

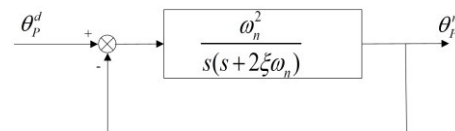The clearance angle φ defined in Eq. (1) is a key design

Fig. 5. The block diagram of the co-actuation module control system. The transfer fiction is simplified as a second-order system.

parameter in implementing the co-actuation approach. To ensure free motion, the clearance angle must be large enough to tolerate the steady-state error ε between desired and real positions of the physical constraint (θ_P^d and θ_P^r), i.e.

$$\varphi > 2\max(\varepsilon)$$
$$\varepsilon = \left|\theta_P^d - \theta_P^r\right|$$
(6)

The lower limit of the clearance angle depends on not only the performance of the control system, but also the maximum speed at which the operator's hand would be allowed to move without resulting in an unintended collision in free motion. This speed is decided during the design phase. A high speed of free motion requires a larger clearance to ensure no collision between the link and the physical constraint during free motion. Therefore, a critical problem in the design of the co-actuation module is to find the lower limit of the clearance angle.

To estimate the maximum error ε, we assume the input signal of the controller for the physical constraint is

$$\theta_P^d = \theta_{in}\sin(\omega t)$$
(7)

The output is

$$\theta_P^r = \theta_{out}\sin(\omega t + \phi)$$
(8)

Then,

$$\varepsilon = \left|\theta_{in}\sin(\omega t) - \theta_{out}\sin(\omega t + \phi)\right|$$
(9)

The reason we chose the sinusoidal function as the input signal is because: 1) in most cases the link rotates within allowable angular range, thus the amplitude of the sinusoidal function can easily be determined; 2) it is intui-
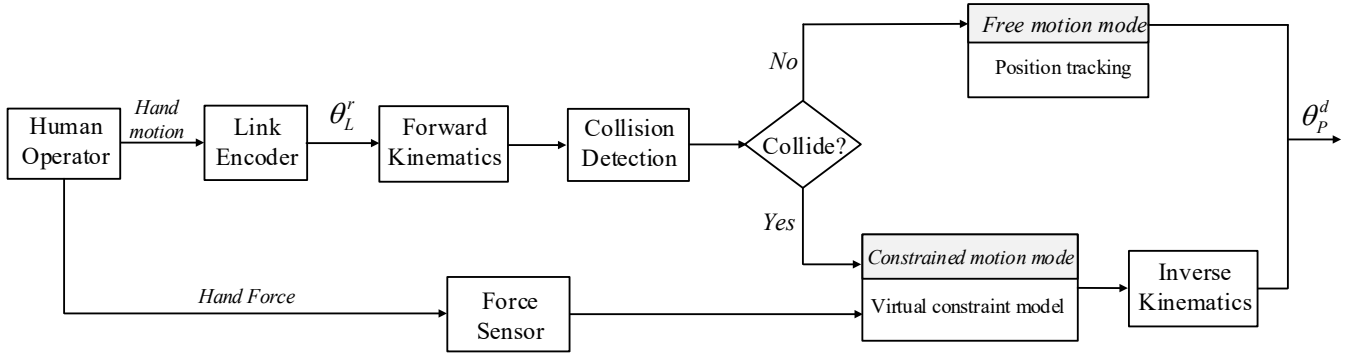
by the user. The major components in the module are listed in TABLE I. In this case, the inertia reduction ratio is η=0.168, which means the effective inertia is reduced by 83.2%. The 1 DOF module achieved a stiffness of 40N/mm measured at the end of the link with a length of 80mm (Fig. 4). It is noted that the force-displacement curve has two segments. The lower stiffness of the first segment was due to mechanical backlash in gear box, which was located between the motor and the socket.

Fig. 6. Control scheme of co-actuation. The superscript *d* and *r* mean *desired* and *real* respectively.

tive to measure the speed of motion by the frequency and the amplitude of the sinusoidal function. 3) the error can be determined using frequency response analysis.

Applying frequency response analysis, we can find the maximum error. To illustrate the principle, we assume the control system of the co-actuation module is a second-order system as shown in Fig. 5. The closed-loop transfer function can be expressed as

$$T(s) = \frac{\omega_n^2}{s^2 + 2\xi\omega_n s + \omega_n^2} \qquad (10)$$

By defining

$$u = \frac{\omega}{\omega_n}, m = \frac{\theta_{out}}{\theta_{in}},$$

we obtain

$$\max(\varepsilon) = \theta_{in}\sqrt{m^2 - 2m\cos(\phi) + 1}$$

$$m = \frac{1}{\sqrt{(1-u^2)^2 + 4\xi^2 u^2}} \qquad (11)$$

$$\phi = -\arctan\frac{2\xi u}{1-u^2}$$

Using Eq. (11), we can calculate the lower limit of the clearance angle. Then the clearance angle φ is selected to be larger than the twice of the maximum steady-state error according to Eq. (6). The system parameters in Eq. (11) can be deduced from experimentally determined frequency response, which is illustrated in Section 5.1.

4 CONTROL APPROACH

When simulating tasks in the virtual environment, the control system of co-actuation approach works in two control modes. The free motion mode is activated when no contact exists between the object and the environment, i.e. in free space. The constrained motion mode is activated when the virtual object contacts the environment, i.e. in constrained space.

Fig. 6 illustrates the control structure of co-actuation. The general control scheme of the co-actuation approach is force-and-position-in and position-out. Both force and position are used as inputs depending on which control

mode is activated.

A virtual environment can be divided into free space and constrained space. How the virtual object is constrained depends on different simulating tasks. Here, we take a virtual wall in 2D space as an example to discuss the control method in free and constrained spaces. The principle of the method is general and can be extended to 3D space.

The virtual wall is defined as

$$f(x, y) = 0 \qquad (12)$$

The free space and constrained spaces can be divided by

$$\begin{cases} f(x, y) > 0 & \text{free space} \\ f(x, y) \le 0 & \text{constrained space} \end{cases} \qquad (13)$$

Consider the force feedback device is a five-bar linkage driven by two co-actuation modules as shown in Fig. 7. Suppose the virtual object a point *Q*, which corresponds to the point *Q* on the device. The coordinate of *Q* is determined by θ_L and denoted by $Q_L(x_L, y_L)$. By substituting the coordinates of $Q_L(x_L, y_L)$ into the function $f(x, y)$, we can identify which mode the controller works, i.e.

$$\begin{cases} f(x_L, y_L) > 0 & \text{free motion} \\ f(x_L, y_L) = 0 & \text{constrained motion} \end{cases} \qquad (14)$$

4.1 Free motion control

In free motion mode, the physical constraint is controlled to track the motion of the link. The control target is the desired gap between the physical constraint and the link. To prevent contact with the physical constraint when users move the link, it is desired to control the link position in the middle of the clearance angle. Then the distance of the link to the right and left sides of the socket is the same, i.e. $\varphi/2$. Therefore, the desired position of the physical constraint is determined by the real position of the link, i.e.

$$\theta_P^d = \theta_L^r \qquad (15)$$

4.2 Constrained motion control

In constrained motion mode, the physical constraint is controlled to simulate the virtual wall according to admit-

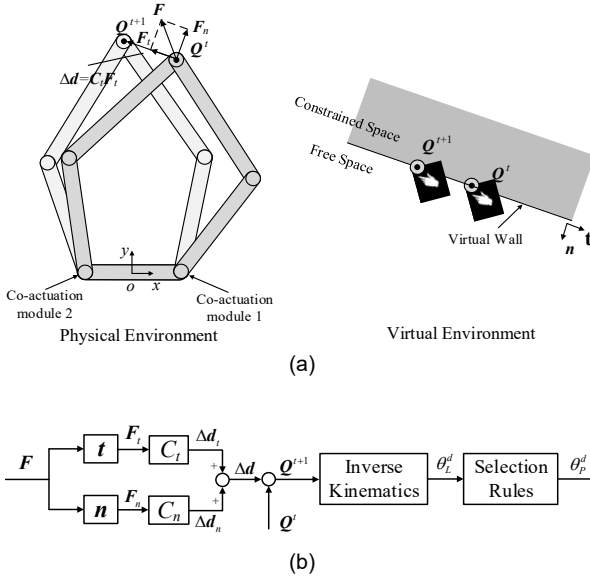Fig. 7. A virtual constraint model. (a) The desired position of the end-effector and corresponding virtual object at time *t*. *n* and *t* indicate the normal and tangential directions of the virtual wall respectively. (b) The control scheme of the constrained motion mode. The selection rules are illustrated in Section 4.4.

tance principle. As presented in Fig. 7 (a), we assume that the point Q represents the position of the end-effector of the device. The point Q in virtual space is the avatar of the end-effector. Assuming at time *t*, the end-effector is in constrained space and collides with the virtual wall. According to the force to end-effector applied by human hand, the desired position of virtual object at time *t+1* is

$$Q^{t+1} = Q^t + \Delta d$$
$$\Delta d = C_t F_t + C_n F_n \quad (16)$$

where C_t and C_n are compliance coefficients in tangential and normal directions of the virtual wall respectively. F_t and F_n are the tangential force and the normal force respectively, which are calculated by,

$$F_t = (F \cdot t)t$$
$$F_n = (F \cdot n)n \quad (17)$$

where F is the force applied to the end-effector by the user, which can be measured by a force sensor. After getting the Q^{t+1}, the desired link angle θ_L^d is obtained, which is used to calculate the desired angle of the physical constraint θ_P^d according to Eq. (2) and selection rules illustrated in Section 4.4. The control scheme discussed above is illustrated in Fig. 7 (b).

To render a high stiffness virtual wall, we choose $C_n = 0$ and $C_t > 0$. The zero C_n ensures that the displacement normal to the wall is zero, so that to simulate a stiff virtual wall. To render the friction on the stiff virtual wall, we use the following equation to determine the desired displacement tangential to the wall:

$$\Delta d_t = C_t F_t \quad (18)$$

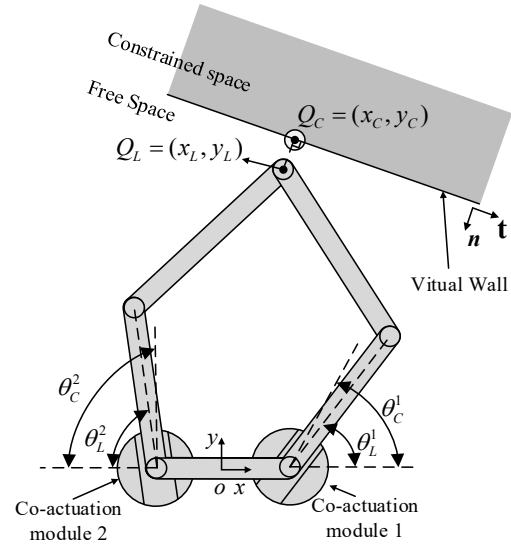C_t can be set according to the requirement of the desired

friction, and increasing the value of C_t results in a decreased friction force F_t. However, the maximum value of C_t is limited by the stability of the controller. When the time interval is set as 0.002 s, we found that the sliding movement is smooth when $C_t < 1.33$ mm/N. This control scheme is different from the traditional admittance control where a non-zero inertial term and viscous damping term are usually included to determine the desired displacement. Due to the decoupling between the link and the motor in the co-actuation approach, the determination of the desired displacement can be simplified without considering the inertial term. During the sliding motion, the user will perceive the inertia of end-effector, but the inertia of motors and transmission gear are not reflected to the user because of the decoupling. Therefore, when moving slowly on the wall, users will perceive a friction force, while moving fast, they will perceive a damping force.

4.3 Switching between two modes

In constrained motion, the link contacts the physical constraint. Since the physical constraint has two contact sides (Fig. 1), to differentiate, we define

$$\theta_C = \begin{cases} \theta_p + \dfrac{\varphi}{2}, & \text{left side contact} \\ \theta_p - \dfrac{\varphi}{2}, & \text{right side contact} \end{cases} \quad (19)$$

which side of contacts should be selected is discussed in Section 4.4.

Suppose $Q_C(x_C, y_C)$ is the position of the virtual object defined by θ_C. The controller switches from free motion mode to constrained motion mode when $Q_C(x_C, y_C)$ is in the constrained space, i.e.

$$if \quad f(x_C, y_C) \le 0, \quad \text{switch to constrained motion} \quad (20)$$

Once the controller switches to the constrained motion, the physical constraint is controlled such that $f(x_C, y_C) = 0$
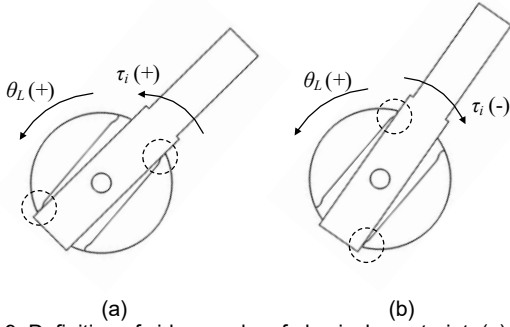

Fig. 8. Switch between control modes.

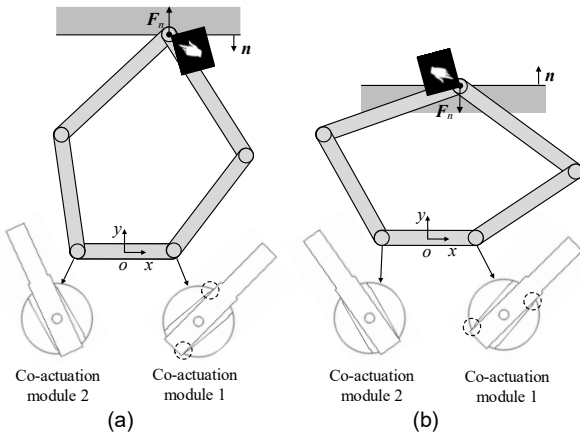Fig. 9. Definition of side + and – of physical constraint. (a) side +. (b) side -.

Fig. 10.   Contact positions of physical constraint: The contact potions in (a) are opposite to that in (b)

even though $f(x_L, y_L) > 0$ at this time. It means that before the link collides to the virtual wall, the physical constraint has been controlled at the proper position to simulate the virtual wall. This is achieved by finding the projection of the point $Q_L(x_L, y_L)$ on the virtual wall as shown in Fig. 8. Before contact, the point $Q_C(x_C, y_C)$ keeps moving on the virtual wall to follow the movement of $Q_L(x_L, y_L)$. During contact, $\theta_C = \theta_L$ and $Q_L(x_L, y_L)$ coincides with $Q_C(x_C, y_C)$, i.e.

$$f(x_C, y_C)=f(x_L, y_L)=0 \tag{21}$$

Therefore, the point $Q_L(x_L, y_L)$ stays exactly on the virtual wall and no penetration happens in theory. In practice, the position of physical constraint is affected by the error and response delay of the control system, as well as backlash in transmission. A small penetration may often exist.

When the virtual object moves back to the free space, the point $Q_C(x_C, y_C)$ keeps staying on the virtual wall, i.e. $f(x_C, y_C)=0$ (see Fig. 8) until the difference between θ_C and θ_L becomes larger than $\varphi / 2$, i.e.

$$if \begin{cases} (x_L, y_L) > 0 \\ |\theta_C - \theta_L| \geq \dfrac{\varphi}{2} \end{cases}, \text{ switch to free motion} \tag{22}$$

Note that in 2D case,

$$\theta_C = \begin{bmatrix} \theta_{C1} \\ \theta_{C2} \end{bmatrix}, \quad \theta_L = \begin{bmatrix} \theta_{L1} \\ \theta_{L2} \end{bmatrix}$$

and the desired position of physical constraint θ_P^d is calculated according to θ_C by Eq. (19) during switch period.

4.4 Selection of contact sides

When the controller works in constrained motion mode, the physical constraint is in contact with the link. Since the contact can occur in two sides of the socket as shown in Fig. 9, which side should be selected needs to be determined.

Suppose the virtual object moves toward the virtual wall. The opposite reaction of normal force F_n is provided by the motor torque τ. According to static equilibrium,

$$\tau = J^{\mathrm{T}} F_n \tag{23}$$

where J denotes a 2x2 Jacobian matrix. The contact position of the physical constraint is determined by:

$$\tau_i \begin{cases} \geq 0 & \text{side+} \\ < 0 & \text{side−} \end{cases} \quad i = 1, 2 \tag{24}$$

where τ_i is the ith element of τ. When the direction of τ_i is the same as that of the link angle θ_L , the contact position of the physical constraint is defined as side +. The definition of the side + and – of the physical constraint is illustrated in Fig. 9. Eq. (23) can be simplified as

$$\tau = J^{\mathrm{T}} n \tag{25}$$

where n is the normal vector against the virtual wall. It suggests that the contact positions are related to the Jacobian matrix, meaning that they depend on the configuration of the device and the normal direction of the virtual wall. Fig. 10 illustrates two cases that the contact positions of the physical constraints are different when the directions of the normal forces are opposite.

5 EXPERIMENTAL VALIDATION

In this section, we validate the effectiveness of co-actuation approach using a 2 DOF haptic device.

As shown in Fig. 11, the 2 DOF haptic device is a five-bar linkage driven by two co-actuation modules. The mechanical and the control parameters of the prototype are listed in TABLE II. To reduce the influence of the backlash in the transmission, a harmonic reducer with a ratio of 50 was used. The two motors were driven by commercial motor drives (Copley ACJ-055-18), which communicated with a computer via a USB-CAN adapter based on CAN-Open protocol with a closed-loop rate of 500 Hz. The motor drivers were operated in 3 kHz for the position and velocity loop and 15 kHz for the current loop. The link angles were measured by two encoders with the resolution of 0.005°, and the encoder signals were processed by a PCI data acquisition card (PCI-1784), which can achieve a sampled frequency higher than 1 kHz. A six-dimensional force sensor (SunRise Inc, M3701) was mounted at the end-effector to measure the force applied
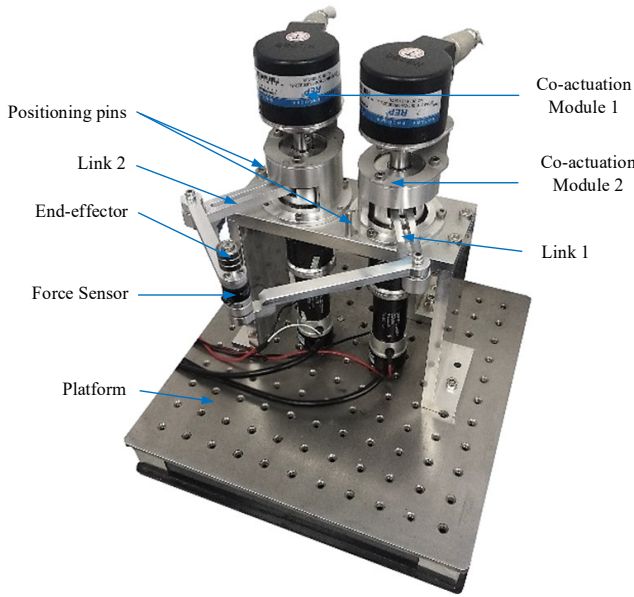
Fig. 11. 2-DOF prototype adopting the co-actuation module.

TABLE II
PARAMETERS OF THE 2 DOF PROTOTYPE

Motor and transmission			
Motor type	Maxon Re 30 268214	Reduction	HarmonicDrive CSF11, ratio 50
Sensors			
Res. of encoders	0.036° (motor), 0.005° (link)	Force sensor	SunRise Inc, M3701, res. 0.01N
Mechanism			
Length of link	90mm(link 1), 110mm(link 2), 74mm(base)	Clearance Angle(φ)	17.04° (module 1), 16.85° (module 2)
Control System			
Drive	Copley ACJ-055-18	Close-loop rate	500Hz
Data acqui-sition card	PCI-1784, >1MHz	Computer	3 GHz Intel Core 2 Duo CPU, 4G RAM
Operating system	Windows 7, 64 bit	Comunicat-ion	USB-CAN adapter, 1Mbps

by the human operator. The signal of the force sensor was uploaded at a rate of 1 kHz to the computer through a USB data acquisition card (SunRise Inc., M8128). The computer used in the experiment is a 3 GHz Intel Core 2 Duo CPU with 4G RAM. All codes were programmed on Visual Studio 2012 and run in Windows 7, 64bit operating system.

The following experiments were implemented within the task workspace of the 2 DOF haptic device, which was defined as a square with the center point at (0 mm, 115 mm) and the length of 100 mm. It was enclosed in the reachable workspace and ensured no singular points of the mechanism. As shown in Fig. 13 (a), a virtual wall was defined as a horizontal line at y=115 mm, and the region
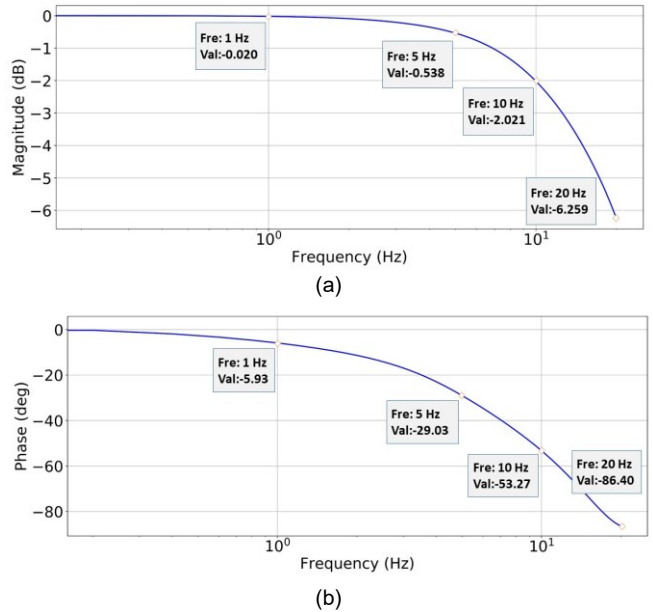

Fig. 12. The experimentally determined Bode diagram of co-actuation module control system. (a) The magnitude-frequency curve. (b) The phase-frequency curve.

above the line (i.e. y >115 mm) was defined as free space.

5.1 Frequency response

The performance of the co-actuation module control system shown in Fig. 5 was investigated by frequency response method. In the experiment, the Copley ACJ drive was operated in position control mode with the following PID parameter values: K_P = 150, K_I=0, K_D=0 in position loop, K_P=0.18, K_I=0.06, K_D=0 in velocity loop and K_P=1.5, K_I=8000, K_D=0 in current loop. The input was the desired angle of physical constraint θ_P^d defined as a sinusoid signal. The real angle of the physical constraint θ_P^r was measured. Empirically, we chose 2 degrees as the input amplitude θ_{in}. We measured the output amplitudes and phase angles at eight input frequencies $\omega/2\pi$ = [1, 2, 3, 5, 7, 10, 15, 20] (Hz). The measurement was repeated for five times at each frequency. The measured Bode diagram of the system is shown in Fig. 12.

Since we approximate the control system by a second-order system, the unknown parameters ω_n and ξ in Eq. (10) can be deduced from the experimentally determined frequency response. Specifically, we implemented system identification and estimated ω_n = 120.9 rad/s, ξ = 0.99. In terms of the step response of the system, the rise time is about 28 ms and no overshoot exists.

The transfer function can be used to calculate the lower limit of the clearance angle using the clearance model proposed in Section 3. In Section 5.2.1, we verified the clearance model based on free motion test.

5.2 Free space performance

Free space performance was evaluated by the maximum speed in free space without collision, back driving force,
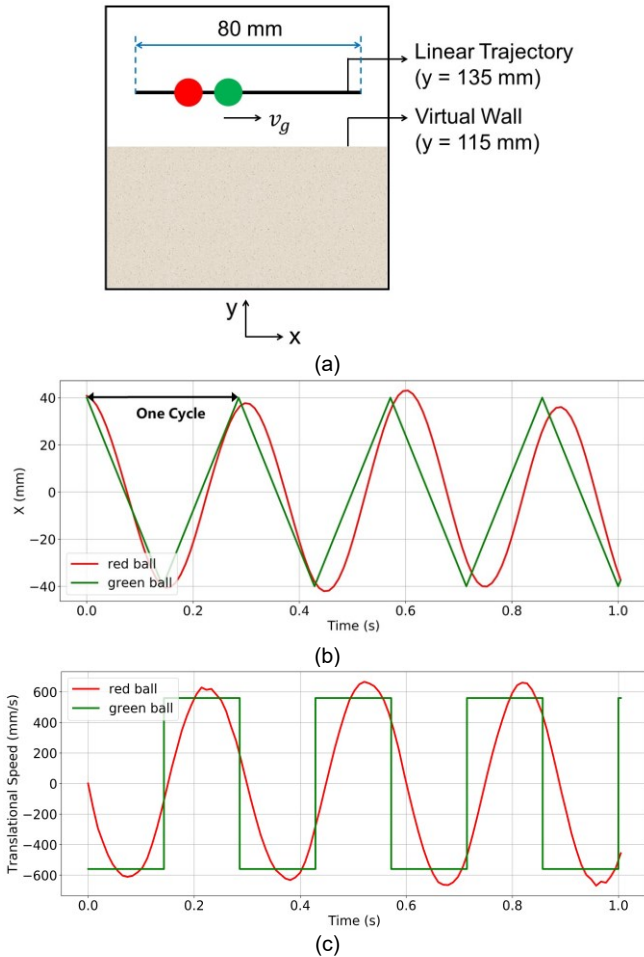
Fig. 13. (a) The graphic display of the virtual environment. (b) The real-time displacements and (c) speeds in X direction of two balls when the red ball tracked the green ball where v_g was set as 560 mm/s.

and effective inertia. During the test, a human operator was asked to move the device along a given trajectory displayed on computer screen. During the motion, the physical constraints were controlled in free motion mode. The link angles and the forces applied by the operator were recorded at the rate of 500 Hz. The speed and acceleration of the motion were estimated using the link encoders.

5.2.1 Collision free speed

To find the maximum speed ensuring no collision in free space, a green virtual ball was displayed on screen to guide the user movement as shown in Fig. 13 (a). The green ball moved back and forth along the linear trajectory at a speed v_g. In programming, the magnitude of v_g is set as a constant value. Once the green ball arrived at the line endpoints, the moving direction reversed instantaneously with the same magnitude of the speed. The operator was asked to move the red ball, i.e. the virtual avatar of the end-effector, to follow the green ball to the best of his/her ability. By varying v_g from 160 to 640 mm/s (one to four cycle per second), the maximum speed ensuring

no collision in free space was found at $v_g = 560 mm/s$. Under this condition, the real-time displacements and speeds in X direction of the red ball were recorded. As shown in Fig. 13 (b) and (c), the actual motion of the red ball was close to a sinusoidal form, when the green ball followed a square wave speed trajectory. On a separate note, the displacements and speeds of the red ball in Y direction, resulted from the error of user motion, were less than 6% and 5% of those in X direction respectively, and were not shown in Fig. 13. The frequency of the red ball motion was observed at about 3.5 Hz.

Solving for inverse kinematics, the link angles corresponding to the above movement was determined as 41 degrees. To verify the clearance model described in Section 3, substituting $\theta_{in} = 41°/2$ (0.358 rad) and 3.5 Hz ($\omega = 7\pi rad/s$) as the input frequency. Based on the obtained transfer function in Section 5.1, it can be calculated that the maximum error ε is about 7.2 degrees. According to Eq. (6), the clearance angle φ should be designed larger than 14.4 degrees.

As shown in TABLE II, we designed the clearance angle φ larger than the lower limit. Therefore, free motion is guaranteed for the specified maximum speed of user movement under the condition of no overshoot.

5.2.2 Effective inertia

The effective inertia can be determined from the system dynamics,

$$F = M_x(\Theta)\ddot{X} + V_x(\Theta,\dot{\Theta}) + G_x(\Theta), \qquad (26)$$

where Θ is the angle vector of joint space coordinates and X is the position vector of Cartesian coordinates. $M_x(\Theta)$ is the inertia matrix of the system formulated in Cartesian coordinates, F is the force vector applied to the end-effector. V_x is the velocity term and G_x is the gravity term. Given a specific position, the maximum inertia can be determined by the largest eigenvalue λ_{max} of $M_x(\Theta)$, i.e.

$$m_e = \lambda_{max}(M_x(\Theta)) \qquad (27)$$

As illustrated in Eq. (3), the effective inertia at end-effector includes only the linkage mass, due to the separation of the link and motor. Thus we obtained the mass and the related geometric parameters using the CAD model of the linkage in Solidworks, and calculated $M_x(\Theta)$ along with λ_{max}. As shown in Fig. 14, the maximum effective inertia forms a symmetrical distribution along the X direction. The maximum effective inertia ranges from 64-142 g within the task workspace.

Furthermore, we implemented experiments to investigate the inertial behavior in two cases: i.e. moving along the given trajectory at a low speed and at a high speed. For the low-speed movement, the back driving force was observed. We chose the line y=115mm, x∈[-40 mm, 40 mm] and the line y=135 mm, x∈[-40 mm, 40 mm] as the desired trajectories. The user moved the end-effector
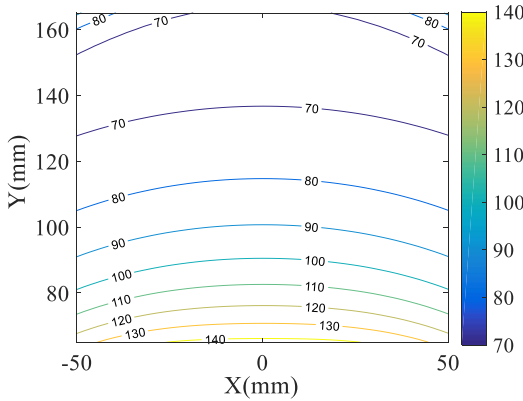
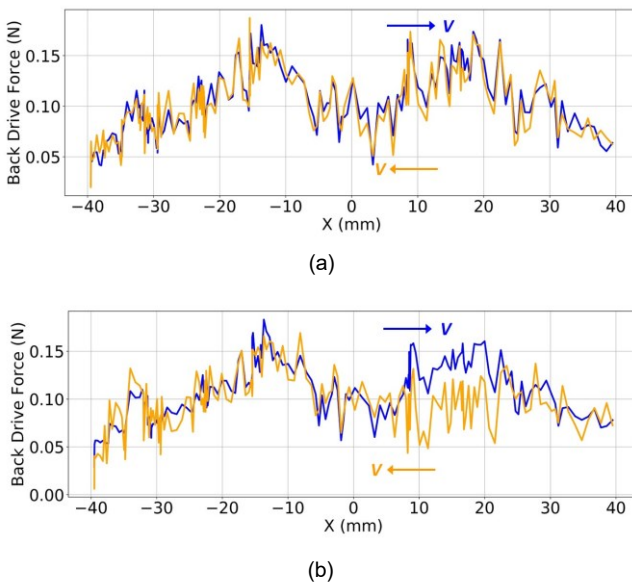Fig. 14. The theoretical value of maximum effective inertia at each position within the task workspace.

(a)

(b)

Fig. 15. The recorded back driving force when moving the end-effector along the linear trajectories at (a) y=115 mm and (b) y=135 mm at a low speed. Blue and yellow curves represent different moving directions.

(a)

(b)

Fig. 16. The experimental effective inertia when moving the end-effector along the linear trajectories at (a) y=115 mm and (b) at y=135 mm. Blue and yellow curves represent different moving directions.

slowly along the two trajectories in free space, while the real-time positions and applied forces were recorded. The results shown in Fig. 15 illustrates that the maximum back driving force is about 0.19 N when moving along the linear trajectory at y=115 mm with the speed ranging from 4.2 to 8.7 mm/s, and 0.19 N moving along the linear trajectory at y=135 mm with the speed ranging from 4.5 to 8.6 mm/s.

For high-speed movement, we also selected these two linear trajectories. The user moved the end-effector fast along the lines. The force applied to the end-effector and the acceleration along the line were measured. It is noted that the measured force includes friction component, which should be subtracted to calculate the inertia. A possible way to estimate the friction component is to measure the back driving force at a low speed that is mainly due to the friction in the linkage joint. Therefore, in each position we subtracted the corresponding back driving force
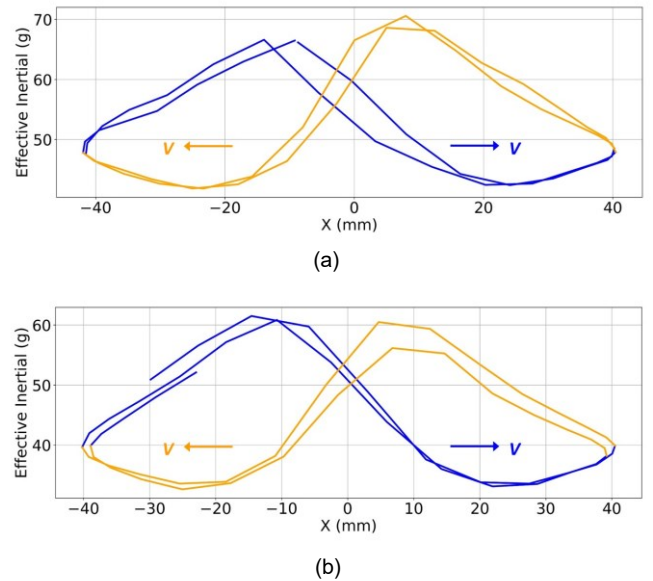
(shown in Fig. 15) from the measured force in high-speed movement, and then divided the resultant force with the acceleration to obtain the inertia. We moved the end-effector along the lines back and forth for several times and the inertia-position curve is plotted as shown in Fig. 16. The effective inertia at y=115 mm is variable from 42 to 71 g when the user speed changed from 50 to 680 mm/s. At y=135 mm, the effective inertia varies from 32 to 62 g when the user speed changed from 48 to 684 mm/s. In addition, the curve is roughly symmetrical along the X direction as well, due to the symmetry of the device mechanism and the moving trajectory.

The effective inertia is anisotropic that varies with the change of the moving direction. The theoretical value in Fig. 14 represents the maximum effective inertia among all directions. For comparison, the theoretical values of effective inertia in X direction along two linear trajectories were calculated, which are close to experimental values as shown in Fig. 16. The maximum error is no more than 4 g.

5.3 Constrained space performance
Constrained space performance was evaluated by penetration and stiffness of virtual wall.

5.3.1 Penetration
To investigate the penetration during contact with a virtual wall, the human operator manipulated the end-effector to simulate two motions: tapping against and sliding along the virtual wall (y=115 mm). The operator taped the virtual wall with gradually increased speeds. As shown in Fig. 17 (a), encountering the virtual wall at a low speed (80 mm/s) produced little penetration (0.02 mm). When striking the virtual wall in high speed (320 mm/s), the penetration increased (0.41 mm) which may
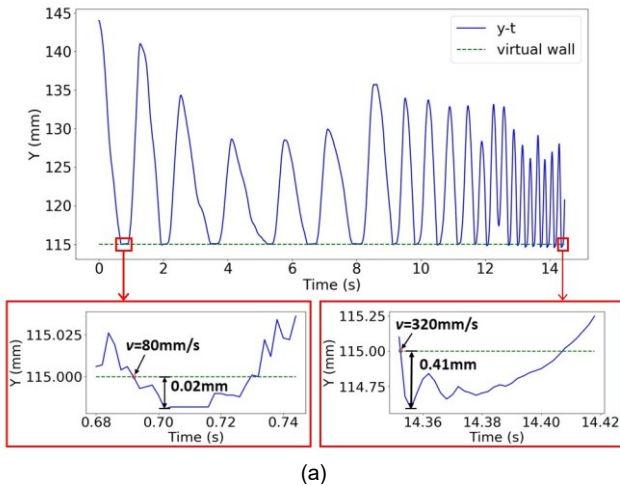
Fig. 17. (a) The recorded displacement of end-effector in Y direction when tapping the virtual wall. (b) The real trajectory of end-effector sliding along the virtual wall back and forth. The *v* with arrow denotes the motion direction.

result from the backlash in transmission and response delay in control system. As shown in Fig. 17 (b), the maximum penetration was approximate 0.13 mm when the operator moved the end-effector back and forth along the virtual wall at an average speed of 42 mm/s.

During tapping and sliding on the virtual wall, the operator felt no detectable chattering. The smooth haptic interaction process was confirmed by the displacement curve shown in Fig. 17, where no high frequency oscillation was found.

The achieved small penetration is due to the advantage of the co-actuation approach. First, the contact position can be anticipated so that the physical constraint can stop exactly on the virtual wall. Secondly, the physical constraints are decoupled from the linkage, reducing the inertia of control system, and thus increases bandwidth. Finally, the virtual wall simulated by physical constraints is passive, which means the physical constraint always stay in the proper position to wait for the collision rather than colliding with the link actively. It greatly prevents chattering during frequent switch between free and constrained spaces.

5.3.2 Stiffness

To evaluate the rendered stiffness of virtual wall, we defined a virtual wall in the task workspace of the device and measured the maximum stiffness at the given posi-
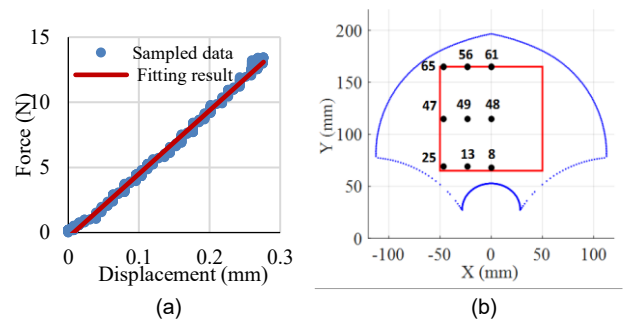

Fig. 18. (a) Force-displacement diagram along negative Y axis at position (-25 mm, 115 mm). (b) The number is the measured stiffness along negative Y axis in the task workspace.

tion. During the test, the physical constraint was controlled according to Eq. (21) to ensure that the end-effector stays on the virtual wall at the given position. A human operator gradually increased the force applied to the virtual wall. The force and the displacement were simultaneously recorded at a rate of 500 Hz. Fig. 18 (a) shows the sample force-displacement curve in one position of the virtual wall at y=115 mm. The measured stiffness was estimated by the slope of the fitting line.

We repeated the above stiffness measurement at different positions. We varied the location of the virtual wall to y=65 mm and y=165 mm and selected three positions, i.e. x=-50, -25, 0 mm, on each virtual wall. A total of nine positions were measured in the left half of the task workspace defined by the red square in Fig. 18 (b). Due to the symmetry of the device, the right half should have the same stiffness property. The numbers shown in Fig. 18 (b) are the stiffnesses at the corresponding positions along the negative direction of Y axis, which range from 8 to 65 N/mm. The lowest stiffness (8 N/mm) happens at the position close to the singularity of the five-bar linkage, which results in significant decrease in force. It is noted that the stiffness may be different along different directions due to non-isotropy of the linkage.

6 DISCUSSION AND CONCLUSION

We have presented a concept of co-actuation for overcoming the limitation of low stiffness of impendence displays and high inertia of admittance displays. The co-actuation approach achieves both high stiffness and low inertia by decoupling the linkages of haptic devices with actuators which move in collaboration with the users' motion. The principle of the approach was tested on both 1-DOF and 2-DOF haptic devices. The experimental results showed that the co-actuation approach can achieve high stiffness comparable to existing admittance displays while having low inertia and back driving force comparable to existing impedance displays. Thus, the approach has potential advantage for the applications requiring both high stiffness and low inertia and back driving force.

Inertia in co-actuation devices is much lower than in traditional admittance displays. Users only feel the linkage inertia due to the decoupling between the link and the motor with transmission. We have shown in 5.2.2 that the maximum effective inertia at the interacting point is 64-142 g within the task workspace. It is possible to reduce the effective inertia by optimizing the linkage design for a particular application.

The co-actuation system can achieve higher bandwidth than traditional admittance displays because the motor only drives a small mass of physical constraint. The link inertia is not the load for the controller. In addition, due to the existence of the clearance, the link can move faster than the physical constraint before making contact with it, which means response delay has less effect in co-actuation system than that in traditional admittance displays.

Penetration to constrained space in co-actuation approach is much less than in traditional impedance approach. In theory, the physical constraint can be controlled to stop exactly at desired position on the boundary of the constrained space. In practice, due to time delay in control system and backlash in transmission, the error of position control exists which may result in small penetration. We have shown a small penetration of 0.02-0.41 mm in Section 5.3.1. It is possible to further reduce the penetration by optimizing response performance in the controller design.

The co-actuation approach relies on the clearance between the physical constraint and the link of the device. The clearance angle is a critical design parameter, which depends on the speed of the link and the response of the controller. A large clearance angle is required for high speed of user motion and low response delay of control system. The proposed clearance model can be used to determine the lower limit of the clearance angle. Free motion can be guaranteed if the clearance angle is larger than the lower limit as long as overshoot in transient process is prevented.

In the case of unilateral constraints, such as the virtual wall, there is no upper limit of the clearance angle. However, in the case of bilateral constraints which is equivalent to moving between two parallel virtual walls, the distance between the two virtual walls is related to the clearance angle. The larger the angle, the larger the distance between the two virtual walls has to be. Because the contact directions on the two simulated virtual walls are opposite, the contact of the link with the physical constraint will change from one side to the other as illustrated in Fig. 10. During the transition, no resistance force can be displayed. Because of this, simulating bilateral constraint, such as peg-in-hole, is challenging for the co-actuation approach. In addition, the compensation of the link gravity using motors is not as easy as in existing admittance displays. Therefore, the proposed approach may have a better fit to the applications requiring small workspace, such as VR-based dental simulator [6]. The ap-

proach may also be applicable to the cases that are more sensitive to large stiffness or force, but less sensitive to the device gravity. Such applications may include virtual fixture in orthopedic surgery, where preventing surface penetration is the most essential performance, and rehabilitation, where large resistant force may be required for arm or leg training.
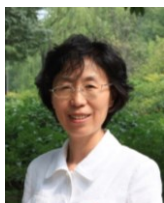
REFERENCES

[1] T. Massie, J. Salisbury, "The PHANTOM haptic interface: a device for probing virtual objects," in ASME Winter Annual Meeting, Symposium on Haptic Interfaces for Virtual Environment and Teleoperator Systems, vol. DSC 55, Chicago, IL, 1994, pp. 295-302.

[2] K. Salisbury, B. Eberman, M. Levin, W. Townsend, "The design and control of an experimental whole-arm manipulator," in The Fifth International Symposium on Robotics Research, 1990, pp. 233-241.

[3] R. Van der Linde, P. Lammertse, E. Frederiksen, B. Ruiter, "The haptic master, a new high-performance haptic interface," in Proceedings of Euro-Haptics, Edinburgh, U.K., 2002, pp. 1-5.

[4] E. Faulring, J. Colgate, M. Peshkin, "The cobotic hand controller: design, control and performance of a novel haptic display," International Journal of Robotics Research, vol. 25, no. 11, pp. 1099-1119, 2005.

[5] http://www.geomagic.com/en/products-landing-pages/haptic.

[6] D. Wang, Y. Zhang, J. Hou, et al, "iDental: a haptic-based dental simulator and its preliminary user evaluation," IEEE Transactions on Haptics, vol. 5, no. 4, pp. 332-343, 2012.

[7] H. Tan, B. Eberman, M. Srinivasan, and B. Cheng, "Human factors for the design of force-reflecting haptic interfaces," in ASME DSC, vol. 55, no. 1, Chicago, IL, 1994, pp. 353-359.

[8] J. E. Colgate, G. Schenkel, "Passivity of a class of sampled data systems: application to haptic interfaces," in Proceedings of the American Control Conference, 1994, pp. 3236-3240.

[9] J. J. Abbott, A. M. Okamura, "Effects of position quantization and sampling rate on virtual-wall passivity," IEEE Transactions on Robotics, vol. 21, no. 5, pp. 952-964, 2005.

[10] N. Diolaiti, G. Niemeyer, F. Barbagli and J. K. Salisbury, "Stability of haptic rendering: discretization, quantization, time delay, and coulomb effects," IEEE Transactions on Robotics, vol. 22, no. 2, pp. 256-268, 2006.

[11] M. Mahvash and V. Hayward, "High-fidelity passive force-reflecting virtual environments," IEEE Transactions on Robotics, vol. 21, no. 1, pp. 38-46, 2005.

[12] M. Zinn, O. Khatib, B. Roth, J.K. Salisbury, "Large workspace haptic devices: a new actuation approach," in Symposium on Haptic Interfaces for Virtual Environment and Teleoperator Systems, 2008, pp. 185-192.

[13] C. Cho, J.B. Song, M. Kim, "Energy-based control of a haptic device using brakes," IEEE Transactions on Systems, Man, and Cybernetics, vol. 37, no. 2, pp. 341-349, 2007.

[14] F. Conti, O. Khatib, C. Baur, "A hybrid actuation approach for haptic devices," in Proceedings of World Haptics Conference, Tsukaba, Japan, 2007, pp. 367-372.

[15] J. An, D.S. Kwon, "Stability and performance of haptic interfaces with

active/passive actuators theory and experiments," International Journal of Robotics Research, vol. 25, no. 11, pp. 1121-1136, 2006.

[16] T. B. Kwon, J. B. Song, "Force display using a hybrid haptic device composed of motors and brakes," Mechatronics, vol. 16, 249-257, 2006.

[17] D. K. Swanson, W. J. Book, "Path-following control for dissipative passive haptic displays," in Proceedings of the 11th Symposium on Haptic Interfaces for Virtual Environment and Teleoperator Systems, 2003, pp. 101-108.

[18] A. Gosline, V. Hayward, "Fddy current brakes for haptic interfaces: design, identification, and control," IEEE/ASME Transactions on Mechatronics, vol. 13, no. 6, pp. 669-677, 2008.

[19] D. W. Weir, J. E. Colgate, M. A. Peshkin, "Measuring and increasing Z-width with active electrical damping," in Proceedings of the Symposium on Haptic Interfaces for Virtual Environment and Teleoperator Systems, 2008, pp. 169-175.

[20] N. Diolaiti，G. Niemeyer，N. A. Tanner, "Wave haptics: Building stiff controllers from the natural motor dynamics," International Journal of Robotics Research, vol. 26, no. 1, pp. 5-21, 2007

[21] W. A. McNeely, "Robotic Graphics, "A New approach to force feedback for virtual reality," Proc. of 1993 IEEE Virtual Reality Annual International Symposium (VRAIS '93), pp. 336-341, 1993.

[22] Y. Yokokohji, N. Muramori, Y. Sato, T. Yoshikawa, "Designing an encountered-type haptic display for multiple fingertip contacts based on the observation of human grasping behaviors," International Journal of Robotics Research, vol. 24, no. 9, pp. 717-729, 2005

[23] H. Kajimoto；N. Kawakami；S. Tachi；I. Kawabuchi, "An encounter-type multi-fingered master hand using circuitous joints", in Proceedings of the 2005 IEEE International Conference on Robotics and Automation, pp. 2667 - 2672

[24] N. Hungr, B. Roger, A. J. Hodgson, C. Plaskos, "Dynamic physical constraints: emulating hard surfaces with high realism," IEEE Transactions on Haptics, vol. 5, no. 1, pp. 48-57, 2012.

[25] J. Song, Y. Zhang, H. Zhang, et al, "Co-actuation: achieve high stiffness and low inertia in force feedback device," in Proceedings of Euro-Haptics, London, UK, 2016, pp. 229-239.

[26] D. A. Lawrence and J. D. Chapel, "Performance trade-offs for hand controller design," in Proceedings of the 1994 IEEE International Conference on Robotics and Automation, San Diego, CA, 1994, pp. 3211-3216.

Hongdong Zhang received the B.S. degree in mechanical engineering from the Beijing Jiaotong University, Beijing, China in 2015, and the M.S. degree in mechanical engineering from Beihang University, in 2018. His research interests include the design, analysis, and control of parallel mechanisms with applications to haptic devices.

Weiliang Xu (SM'99) received the B.E. degree in manufacturing engineering and the M.E. degree in mechanical engineering from Southeast University, Nanjing, China, in 1982 and 1985, respectively, and the Ph.D. degree in mechatronics and robotics from the Beijing University of Aeronautics and Astronautics, Beijing, China, in 1988. He was with the City University of Hong Kong, University of Stuttgart, Southeast University, and Massey University. Since 2011, he has been with The University of Auckland, New Zealand, where he is currently the Chair of Mechatronics Engineering. His current research interests include advanced mechatronics/robotics with applications in medicine and food. Dr. Xu was an Associate Editor of the IEEE Robotics and Automation Magazine from 2008 to 2009. He has served as an Associate Editor of the IEEE Transactions on Industrial Electronics from 2003 to 2019.

Jee-Hwan Ryu (M'02) received the B.S. degree in mechanical engineering from Inha University, Incheon, South Korea, in 1995, and the M.S. and Ph.D. degrees in mechanical engineering from the Korea Advanced Institute of Science and Technology, Taejon, South Korea, in 1995 and 2002, respectively. He is currently a Professor with the Department of Mechanical Engineering, Korea University of Technology and Education, Cheonan, South Korea. His research interests include haptics, telerobotics, teleoperation, exoskeletons, and autonomous vehicles.

Ruihang Chu received the B.E. degree in mechanical engineering and automation from Beihang University, Beijing, China in 2017. Currently he is working towards a M.E. degree in School of Mechanical Engineering and Automation at Beihang University, Beijing, China. His research interests include haptics, human-machine interaction, virtual prototyping, and robotics.

Dangxiao Wang (M'05-SM'13) received a Ph.D. degree in mechanical engineering from Beihang University, Beijing, China in 2004. Currently he is a Professor at the State Key Laboratory of Virtual Reality Technology and Systems in Beihang University. From 2004 to 2006, he was a post Doc at Beihang University. From 2006 to 2016, he was an Assistant and Associate Professor in the School of Mechanical Engineering and Automation, Beihang University. His research interests include haptic rendering, neurohaptics and medical robotic systems. He had been the chair of Executive Committee of the IEEE Technical Committee on Haptics (IEEE TCH) from 2014 to 2017.

Yuru Zhang (M'95-SM'08) received the Ph.D. degrees in mechanical engineering from Beihang University, Beijing, China in 1987. Currently she is leading the Division of Human-Machine Interaction at the State Key Laboratory of Virtual Reality Technology and System. Her technical interests include haptic human-machine interface, medical robotic system, robotic dexterous manipulation, and virtual prototyping. She is an associate editor of IEEE Robotics and Automation Letters.